# The inertial regime of drop impact on an anisotropic porous substrate

## H. Ding[1,2]† and T. G. Theofanous[1]

[1] Department of Chemical Engineering, University of California at Santa Barbara, CA 93106-5080, USA

[2] Department of Modern Mechanics, University of Science and Technology of China, Hefei, China

Axisymmetric droplet impact on a hydrophilic substrate with one pore of relatively large radius is numerically studied using diffuse-interface methods. The flows above the substrate and in the capillary are fully resolved by a Navier–Stokes solver that accounts for contact-angle hysteresis. Upon impact, the infiltration of the drop into the capillary is seen to follow one or more of the three regimes identified in recent experiments (Delbos, Lorenceau & Pitois, *J. Colloid Interface Sci.*, vol. 341, 2010, p. 171): complete penetration, partial penetration as a slug, and re-entry with bubble entrapment. The agreement on experimentally measured quantities, such as transition criteria and slug lengths, is quantitative. On this basis we reveal previously unidentified flow phenomena, investigate flow details that are not accessible experimentally, expand the parameter space considered previously, identify the key asymptotic regimes in the penetration transient, generalize the results in terms of relevant dimensionless groups, and provide a further step (using a multi-capillary arrangement as an idealization of a porous substrate) towards the ultimate purpose of such work, which is the understanding of inertial effects with porous substrates, including eccentric impacts. The significant effect of impact inertia is revealed as a spatial anchoring of a stagnation region, formed and persisting for most of the transient. As a consequence, fluid within an upright cylinder is destined to enter the capillary, and this is in agreement with the hypothesis of Delbos *et al.* in interpreting the amounts of liquid found inside the capillary, except that the radius of the cylinder is 30 % greater than the capillary radius. The remainder of the liquid spreads laterally on the substrate surface, and the slug regime is a consequence of this partition. Numerical experiments also indicate that after reaching the maximum-spread area, the lamella on the substrate tends to refill the capillary and entrap a bubble, unless contact-angle hysteresis hinders the radially inward motion of the lamella.

**Key words:** capillary flows, contact lines, drops

---

## 1. Introduction

Previous work on liquid-drop contact with porous substrates has mainly addressed the creeping-flow regime ($Re = \rho V R/\mu \ll 1$), as it is found with sufficiently small contact velocities $V$, sufficiently high viscosities $\mu$, and/or sufficiently fine pore sizes $R$

† Email address for correspondence: hding@ustc.edu.cn

(Clarke *et al.* 2002; Lembach *et al.* 2010). At such conditions the spreading (onto the substrate by lubrication mechanics) and infiltration (into the substrate by Darcy flow) processes can be formulated independently, accounting for contact-line and capillary-pressure effects, and the solution is obtained by matching the infiltration rates and pressures across the common boundary of their respective spatial domains (Denesuk *et al.* 1993; Davis & Hocking 1999, 2000; Holman *et al.* 2002; Alleborn & Raszillier 2004; Hilpert & Ben-David 2009). When inertia is not negligible, these simplifications are no longer tenable, and the kinds of experimental data, numerical simulations, and theory needed to elucidate the key physics of this regime are not yet available. On the other hand, recent experiments of drop impact on patterned substrates displayed a variety of drop dynamics, for example, simultaneous spreading inside and above a textured surface (Sivakumar *et al.* 2005), various deposition shapes on a wettability-patterned surface (Lee, Chang & Kim 2010), and predominant splashing directions (Xu 2005). These findings suggest the potential of using microfabricated rough surfaces to design drop behaviours after impact, which, however, needs systematic numerical simulation to identify the underlying crucial physics. Besides the obvious basic interest in bringing the drop-impact problem to completion, there is also substantial motivation from a recent practical need to understand the fate of certain threat agents in the environment, or on protective clothing (Defense Threat Reduction Agency, Workshop in Integrative Approaches to Threat Agent Fate in the Environment, Santa Barbara, April 23, 2010). An initial approach to this problem has been provided by experiments performed with the elementary geometry of a substrate with a single capillary (Kogan, Johnson & Schumacher 2008; Delbos, Lorenceau & Pitois 2010). In this paper we take the next few steps with the help of direct numerical simulations based on interfacial mechanics, modelled by the diffuse-interface method.

The principal results of the work of Delbos *et al.* with inertia-impact on hydrophilic substrates (they also considered hydrophobic conditions, which are outside our present focus) is that the volume of the liquid that enters the capillary corresponds to the portion of the drop right over the capillary (enclosed within an upright cylinder with the same diameter). This slug formation was found to occur above a certain critical velocity, the magnitude of which diminished with increasing capillary radius. The remainder of the liquid in the drop simply spread out on the surface of the substrate. They also presented displacement histories, and thereby penetration velocities are also available. Such penetration-rate data are also available from the work of Kogan *et al.* (2008). These authors note certain 'curiosities': (*a*) slug velocities that are higher than the impact velocities, and (*b*) penetration rates that required higher than stagnation pressures at the capillary inlet to conform to the experimental data (they hypothesized that these higher values were due to water-hammer-like shocks created by the impact).

When the impact velocity is not high enough, and when contact-angle hysteresis is not present, the spread-out lamella can rebound back towards the capillary and re-enter, thereby entrapping the gas already in the capillary, behind the liquid slug (the bubble regime in the terminology of Delbos *et al.*). Finally, at sufficiently low velocities ($Re < 1$), there is sufficient time (relative to spreading) for all the liquid to be absorbed into the capillary, yielding the total penetration regime.

In this paper we demonstrate the feasibility and efficacy of predicting the above experimental findings by fully resolved solutions of the Navier–Stokes equations. Moreover, having validated our method we employ the simulations to reveal previously unidentified flow phenomena, investigate flow details that are not accessible experimentally, expand the parameter space considered in the experiments, identify the key asymptotic regimes in the penetration transient, generalize the results in terms

of relevant dimensionless groups, and provide a further step (using a multi-capillary arrangement as an idealization of a porous substrate) towards the ultimate purpose of such work, which is the understanding of inertial effects with porous substrates, including eccentric impacts.

We use a diffuse-interface method (Jacqmin 1999; Ding, Spelt & Shu 2007). The flows, both above the substrate and in the capillary, are resolved by solving the Navier–Stokes equations (Ding *et al.* 2007). The evolution of the fluid–fluid interface is governed by the convective Cahn–Hilliard equation (Jacqmin 1999). The stress singularity at moving contact lines is relieved using a diffuse-interface model (Seppecher 1996; Jacqmin 2000) and a geometric formulation of the wetting condition is implemented (Ding & Spelt 2007*b*). The chemical inhomogeneities and roughness are assumed to be uniform on the solid substrate and modelled by a window of contact-angle hysteresis (Ding & Spelt 2008).

The paper is organized as follows. The problem statement and the details of numerical methods are presented in § 2. In § 3 we first numerically reproduce the three penetration regimes with similar flow parameters to the experiments, and therefore validate our methods; then we present the penetration regime map in the expanded parameter space and discuss the flow phenomena, droplet ejection, and related fluid mechanisms. After that we analyse the phenomena of penetration associated with the significance of inertia in § 4, revealing a spatial anchoring of a stagnation region, formed and persisting for most of the transient. We analyse the regime transitions in § 5, and in particular, find that contact-angle hysteresis hinders the radially inward motion of the lamella, and effectively prevents the refilling of the capillary. In § 6 we investigate the infiltration dynamics through a scaling argument. A further step, i.e. using an embedded annular capillary arrangement as an idealization of a porous substrate, is attempted in § 7.

## 2. Problem statement and numerical methods

### 2.1. *Problem statement*

We consider here a spherical liquid drop of radius $a$ impacting on a solid substrate with an open-ended hole of radius $R_t(= r_t a)$ (figure 1). The drop is placed slightly above the solid substrate, and allowed to fall with an initial speed $U$. The viscosity and density of the drop are $\mu$ and $\rho$, respectively, and the ratio of viscosity (density) of the surrounding fluid to that of the drop is denoted by $\lambda_\mu$ ($\lambda_\rho$). The two fluids involved here are liquid and air, and the typical value of $\lambda_\mu(\lambda_\rho)$ is 0.05 (0.001). The surface tension coefficient $\sigma$ is assumed to be constant. The equations of motion are the Navier–Stokes equations with the divergence-free constraint. We render the equations of motion dimensionless by choosing $a$, $U$ and $\tau(= a/U)$ as the characteristic length, velocity and time scales, respectively:

$$\bar{\rho}\left(\frac{\partial \boldsymbol{u}}{\partial t} + \boldsymbol{u} \cdot \nabla \boldsymbol{u}\right) = -\nabla p + \frac{1}{Re}\nabla \cdot [\bar{\mu}(\nabla \boldsymbol{u} + \nabla \boldsymbol{u}^{\mathrm{T}})] + \frac{\boldsymbol{f}_s}{We} - \frac{\bar{\rho}}{Fr}\boldsymbol{j}, \qquad (2.1)$$

$$\nabla \cdot \boldsymbol{u} = 0, \qquad (2.2)$$

where the dimensionless viscosity and density are $\bar{\mu} = C + (1 - C)\lambda_\mu$ and $\bar{\rho} = C + (1 - C)\lambda_\rho$, respectively, and $C$ is the volume fraction of one of the fluids ($0 \leqslant C \leqslant 1$). The dimensionless groups are the Reynolds number $Re = \rho U a/\mu$, Weber number $We = \rho U^2 a/\sigma$, and Froude number $Fr = U^2/(ga)$, where $g$ is gravitational acceleration. We shall also refer to the Ohnesorge number $Oh = \sqrt{We}/Re = \mu/\sqrt{\rho \sigma a}$, and the capillary number $Ca = We/Re = \mu U/\sigma$. The symbol $\boldsymbol{f}_s$ denotes the dimensionless
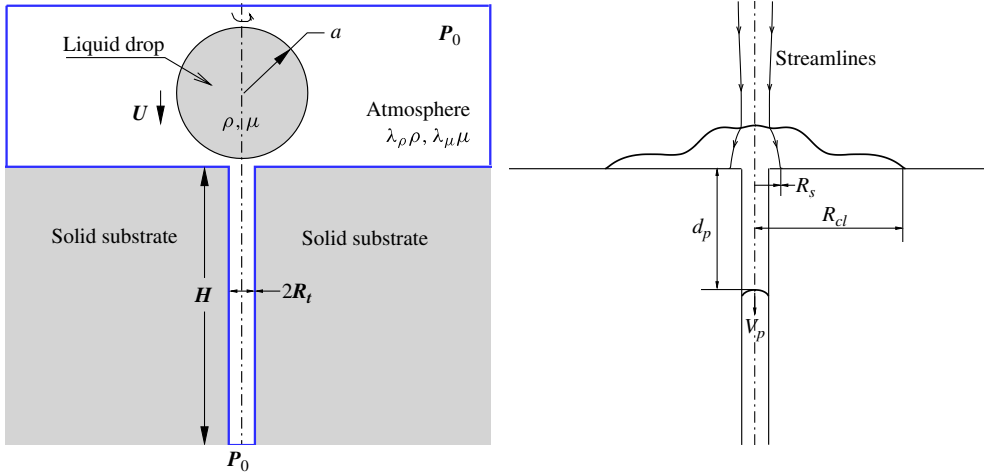
FIGURE 1. (Colour online available at journals.cambridge.org/flm) Geometric definition of the problem and related nomenclature. $R_s(=r_s a)$ is the radius of the limiting streamline that separates flow entering the capillary from flow spreading outwards.

surface tension force and $\boldsymbol{j}$ denotes the vertical unit vector. The dimensionless numbers on the capillary length scale are $Re_r(=r_t Re)$ and $We_r(=r_t We)$.

All calculations reported here are carried out in the $(r, z)$ plane. Because of axisymmetry only half of the flow domain in figure 1 is considered in computation. The domain consists of a upper subdomain of $5 \times 3$ and a lower subdomain of $r_t \times 8$, wherein the heights and widths of the subdomains are chosen in such a manner that the effect of the domain size is negligible, which has been confirmed by numerical experiments. A uniform mesh size $h$ of 0.01 is used if not stated otherwise. The boundary conditions for the velocity components $(u_r, u_z)$, where the subscripts $r$ and $z$ denote the respective directions, are imposed as follows: no-slip at the solid walls; $u_r = 0$ and $\partial u_z / \partial r = 0$ at the axis of axisymmetry; $\partial \boldsymbol{u} / \partial z = 0$ at the top and bottom boundaries; $\partial \boldsymbol{u} / \partial r = 0$ at the right boundary of the upper subdomain. The pressure at the lower open end of the capillary is set equal to the value at the far field, $p_0$, which is approximated by the pressure at the right upper corner of the domain (see figure 1); $\partial p / \partial \boldsymbol{n} = 0$ at the other boundaries, where $\boldsymbol{n}$ is normal to and pointing to the corresponding boundary. The initial velocity field inside the drop is set to $-1$, whereas outside the drop it is set to zero.

## 2.2. *The diffuse-interface method and wetting conditions*

We use volume fraction $C$ to describe the interface and its evolution in the framework of a diffuse-interface model (Ding *et al.* 2007): a sharp interface separating the two fluids is replaced by an interfacial region of finite thickness such that the jumps in density and viscosity, as well as the pressure field, are smoothed to a certain degree across the interface. The time evolution of the $C$ field is governed by the convective Cahn–Hilliard equation

$$\frac{\partial C}{\partial t} + \boldsymbol{\nabla} \cdot (\boldsymbol{u} C) = M \nabla^2 \psi, \tag{2.3}$$

where $M$ is the mobility, and $\psi(= \phi'(C) - \epsilon^2 \nabla^2 C)$ is the chemical potential; $\epsilon$ represents a dimensionless measure of the thickness of diffuse interface, and $\phi = C^2 (1 - C)^2 / 4$ is the bulk energy density. Then, the surface tension force $\boldsymbol{f}_s$
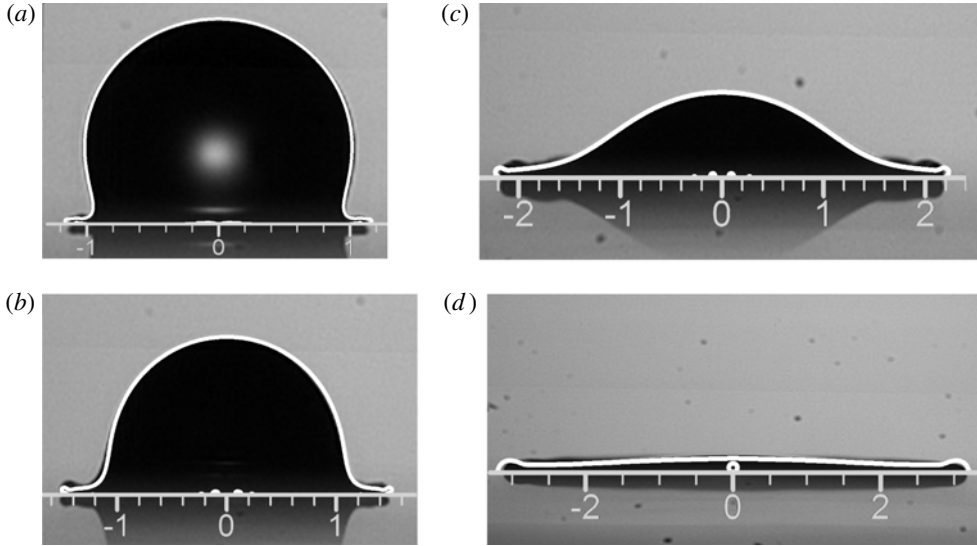
FIGURE 2. Numerical simulation of Center for Risk Studies and Safety experiment (V. Mitkin, private communication) at $We = 164$, $Re = 457$, $\theta_A = 46°$ and $\theta_R = 13°$, at times $t = 0.33$, 0.55, 1.32, and 3.95 ($a$–$d$). The images represent experimental results, and the lines on the images represent numerical results.

in the momentum equation (2.1) can be written as $f_s = 6\sqrt{2}\psi\nabla C/\epsilon$. For accuracy it is required that $\epsilon \ll 1$ and we use $\epsilon = 0.55h = 0.0055$. The model allows for moving contact lines, and by the use of diffusive fluxes it alleviates the related non-integrable stress singularity (Jacqmin 2000). The capillary is assumed to have the same wettability as the solid substrate, which is prescribed by an advancing contact angle $\theta_A$. In some simulations, a moderate contact-angle hysteresis $\Delta\theta (= \theta_A - \theta_R)$ is used to account for the effect of surface roughness and inhomogeneities of the solid substrate. A geometric formulation is used for a prescribed contact angle $\theta$ (Ding & Spelt 2007$b$), leading to boundary conditions for $C$ at the solid walls:

$$\boldsymbol{n} \cdot \nabla C = - \tan\left(\frac{\pi}{2} - \theta\right) |\nabla C - (\boldsymbol{n} \cdot \nabla C)\boldsymbol{n}|. \tag{2.4}$$

For substrates with contact-angle hysteresis, we first estimate the local contact angle $\theta_0$ from the distribution of $C$ at each time step, and then update the value of $C$ at respective ghost cells (located inside the substrate) by (2.4) if $\theta_0$ is outside the hysteresis window, i.e. $\theta = \theta_A$ if $\theta_0 > \theta_A$ and $\theta = \theta_R$ if $\theta_0 < \theta_R$; otherwise we keep the value of $C$ at the ghost cell unchanged (Ding & Spelt 2008). At the sharp edge of the capillary, the value of $C$ at the corresponding ghost cell could be determined both by the wetting conditions of the substrate and the capillary; therefore an averaged value of $C$ is used to avoid this situation.

### 2.3. *Code validation*

The methods and numerical tools employed in this work have been previously validated in the context of drop-spreading on impermeable substrates (Ding & Spelt 2007$a$). The focus was the inertia regime found with capillarity-induced, fast-spreading sessile drops. As an initial step in the present study we extended this experience for impacts on impermeable smooth substrates as illustrated in figure 2. A further
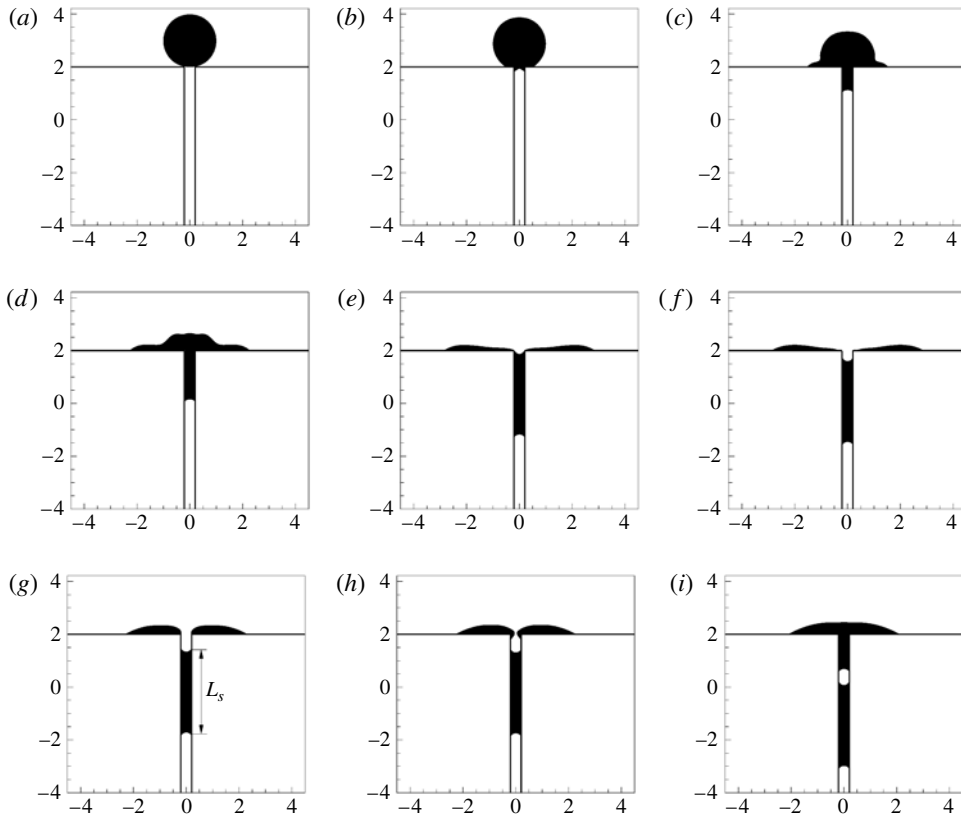
FIGURE 3. A typical case of the regime of re-entry with bubble entrapment. $Re = 311$, $We = 155$, $r_t = 0.2$, $\theta_A = \theta_R = 30°$. Snapshots at $t = 0, 0.11, 0.65, 1.62, 3.78, 4.91, 17.8, 20.2, 25.6$ $(a–i)$.

extension is made in the present work in the still more complex problem regimes found experimentally for drop impacts on capillary-bearing substrates.

## 3. The regimes of penetration

The flows can be classified according to the interaction between the spreading on the solid substrate and the penetration in the capillary. Figure 3 shows a typical example characterized by two penetration phenomena in the capillary: the formation of a cylindrical liquid column (or 'slug') and the re-entry with a bubble entrapped at a later time. This regime has been identified in experiments by Delbos *et al.* (2010) and is referred to here as 're-entry with bubble entrapment'. The three periods of infiltration can be seen from the transitions in penetration distance and velocity ($d_p$ and $V_p$ respectively) in figure 4. They are inertial penetration (figure 3$a$–$e$), slug motion (figure 3$e$–$h$) and bubble entrapment (figure 3$h$–$i$), respectively. The other two regimes observed in the experiments are complete penetration and partial penetration as a slug, which are also found in our simulations. In the regime of partial penetration as a slug, the flow reversal on the substrate and re-entry are missing. In the regime of complete penetration, the whole drop is infiltrated into the capillary in the absence of fluid rupture at the edge of the capillary inlet.
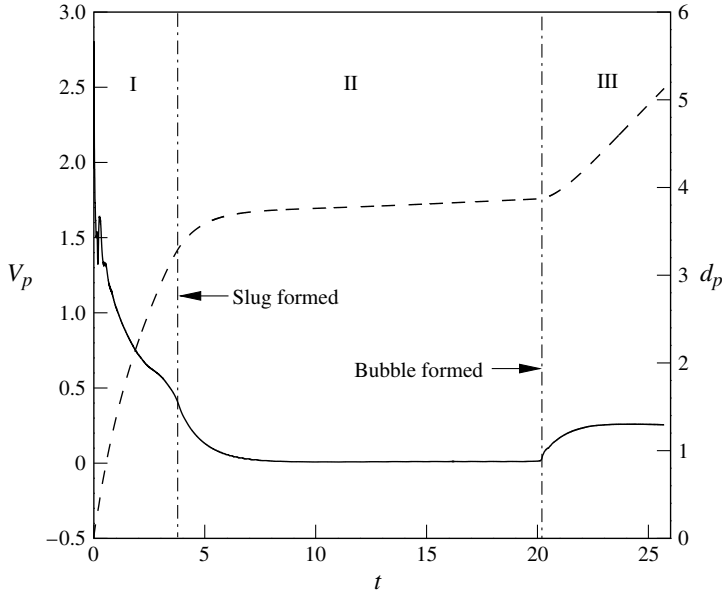
FIGURE 4. Detailed results from the simulation of figure 3. The notations I, II and III represent the periods of forced impregnation, slug motion and bubble entrapment, respectively. The solid line represents the results for the infiltration velocity ($V_P$) and the dashed line shows the depth of penetration ($d_P$).
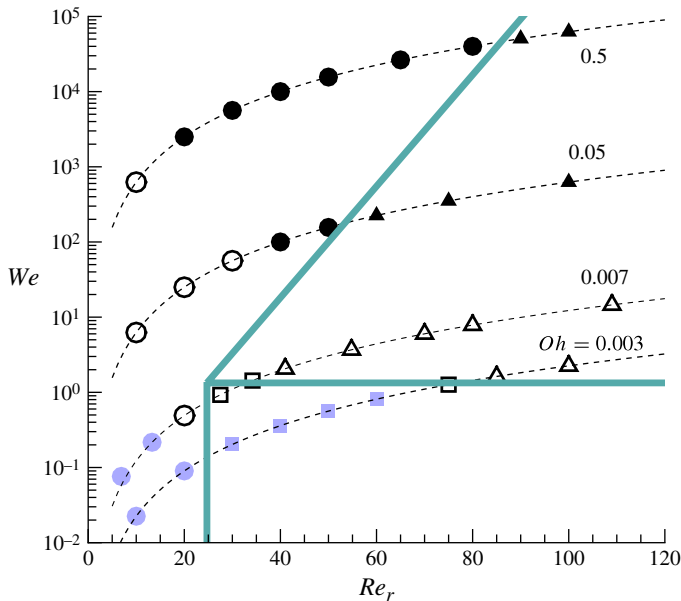


FIGURE 5. (Colour online) Penetration regime map, for $r_t = 0.2$, $\theta_A = 40°$ and $\theta_R = 20°$. The circles represent the cases in the complete penetration regime, the squares show partial penetration as a slug, and the triangles show re-entry with bubble entrapment. Filled symbols represent the cases accompanied by drop pinch-off: black inside the capillary, grey (blue) above the capillary. The thick straight lines represent the approximate boundaries that delineate the three regimes.
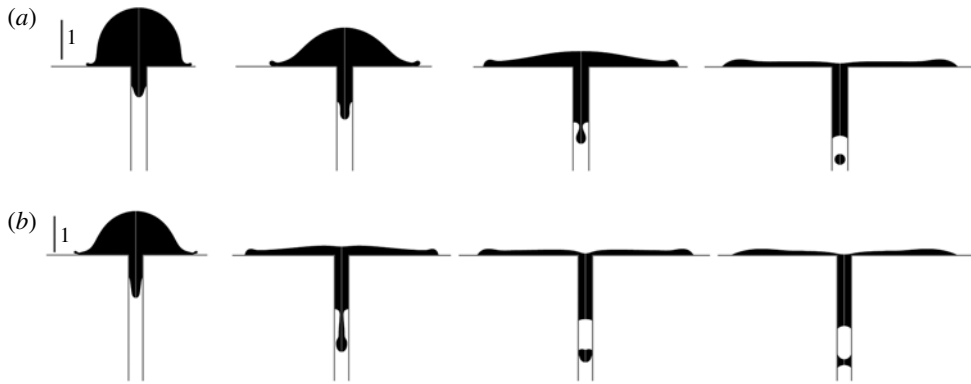
FIGURE 6. Droplet ejection inside the capillary, for $r_t = 0.2$, $\theta_A = 40°$, $\theta_R = 20°$. (*a*) $We = 100$, $Re_r = 40$ and $t = 0.54, 1.14, 2.34, 5.94$. (*b*) $We = 156$, $Re_r = 50$ and $t = 0.84, 2.94, 4.74, 16.14$. Both (*a*) and (*b*) are in the complete penetration regime.

A representative regime map is shown in figure 5. The values of *Oh* are also indicated to delineate the inviscid conditions $0.003 \leqslant Oh \leqslant 0.007$ addressed by Delbos *et al.* (2010) and the extension to viscous conditions obtained by numerical simulations.

We can see that the whole map is anchored at the point ($We \sim 1$, $Re_r \sim 25$). For $We < 1$, the critical condition that separates complete penetration from isolated slug is at $Re_{r,c} \sim 25$. For $We > 1$, the complete penetration region expands with increasing $Re_r$, $\log We_c \sim (Re_r - 25)/14$, and the slug is followed by bubble entrapment. A second-order structure is also evident: for $We < 1$, droplet pinch-off can occur above the capillary, while for $We > 1$ such pinch-off may be found at the nose of the slug within the capillary. Remarkably, increasing viscosity (*Oh*) proves increasingly resistant to slug separation.

Typical examples of droplet pinch-off within the capillary are shown in figures 6 and 7 and above the capillary in figure 8. Impact inertia greatly bends the slug front near the contact line and causes the middle of the interface to protrude; as a result the slug front develops into a liquid ligament, which is pinched off from the slug and forms an ejected droplet. More impact inertia can result in a longer liquid ligament with a larger volume before rupture. Thus the droplet that develops from the pinched ligament has a larger diameter than the capillary, and would then wet the capillary and entrap a bubble simultaneously (figure 6*b*). With sufficiently large inertia the scenario is even more dramatic. A very elongated liquid thread may form, which then pinches off from the slug, and breaks up further into a row of small droplets at a later time due to Rayleigh instability (figure 7). With reference to figure 8(*a*), the rapid spreading on the substrate stretches the drop horizontally, leading initially to a column-like shape and eventually to a pinching neck at the bottom of the column. This series of events is dominated by strong travelling capillary waves, which are induced by wetting rather than by the impact. This phenomenon has also been seen in experiments, e.g. figure 1(*d*) in Delbos *et al.* (2010), as well as in drop impact on impermeable substrates (Roux & Cooper-White 2004; Rioboo *et al.* 2006) and partial coalescence of a drop at a liquid–liquid interface (Blanchette & Bigioni 2006; Zhang, Li & Thoroddsen 2009). The size of the daughter droplet was not reported by Delbos *et al.* (2010); however, our simulations predict that it is about 51 % of the original drop in radius, close to
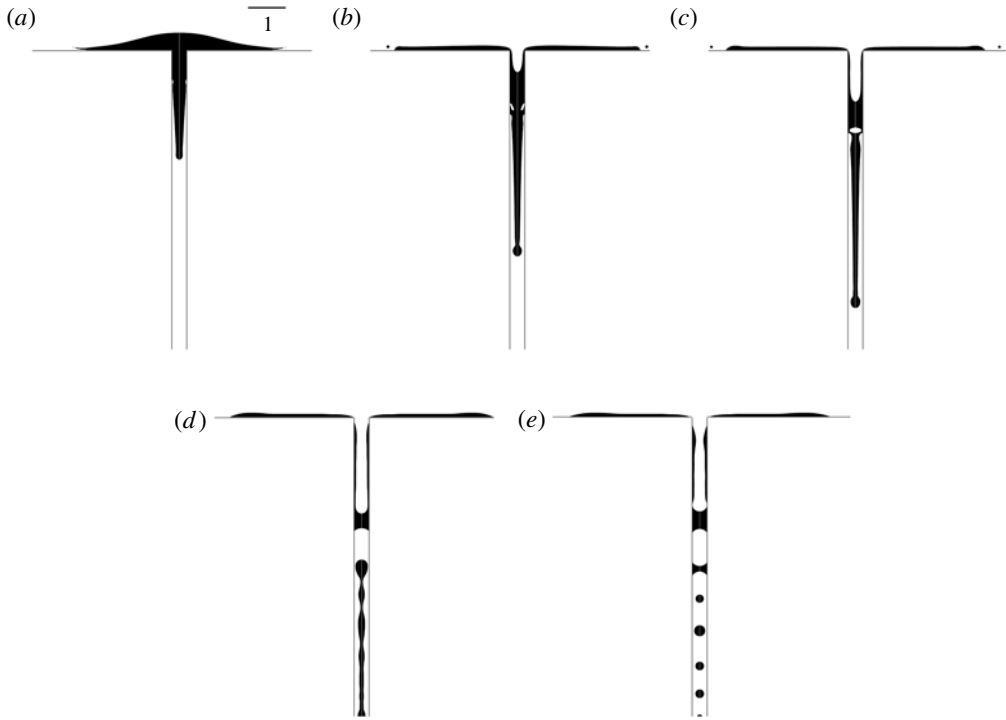
FIGURE 7. Droplet ejection inside the capillary with multiple pinch-offs, for $We = 625$, $Re_r = 100$, $r_t = 0.2$, $\theta_A = 40°$, $\theta_R = 20°$ and $t = 2.04, 4.74, 7.14, 20.04, 33.54$ (*a–e*).

experimental observations by Ding *et al.* (2011), as well as in the partial coalescence of liquid drops (Blanchette & Bigioni 2006; Zhang *et al.* 2009). Figure 8(*b*) shows that the droplet ejection may be accompanied by the occurrence of flow rupture at the capillary inlet. The subsequent coalescence of the droplet with the lamella on the substrate entraps a bubble in the capillary, clearly by a different process from the regime of re-entry with bubble entrapment, which, though, happens at a later time and entraps the second bubble in the capillary.

Inertia plays an important role in the processes of the two drop pinch-offs. However, the underlying mechanisms in the two droplet pinch-offs are so different that it is impossible to have both of them simultaneously. In the droplet pinch-off above the capillary, inertia of fast spreading arises mainly from the conversion of surface energy into kinetic energy (Biance, Clanet & Quéré 2004), rather than the impact inertia, which has an adverse effect on the pinch-off, as shown in the experiments by Roux & Cooper-White (2004); as a result drop pinch-off above the substrate mainly occurs for $We < 1$. Besides this, the pinch-off is related to the propagation and reflection of strong surface waves that start from the moving contact line, which suggests that inertial and surface tension forces must be dominant over viscous force, i.e. occurring at relatively low *Oh*. Comparatively, it requires much more impact inertia to eject a droplet inside a capillary ($We \sim 100$, at least in figure 5). The elongation of the front of the liquid column starts from the interface bending down near the contact line, where essentially the shear stress balances the surface tension force, and the process is characterized by the capillary number. In the case shown in figure 6(*a*), $Ca = 0.5$, which appears to be sufficiently large for the shear to deform the slug front.
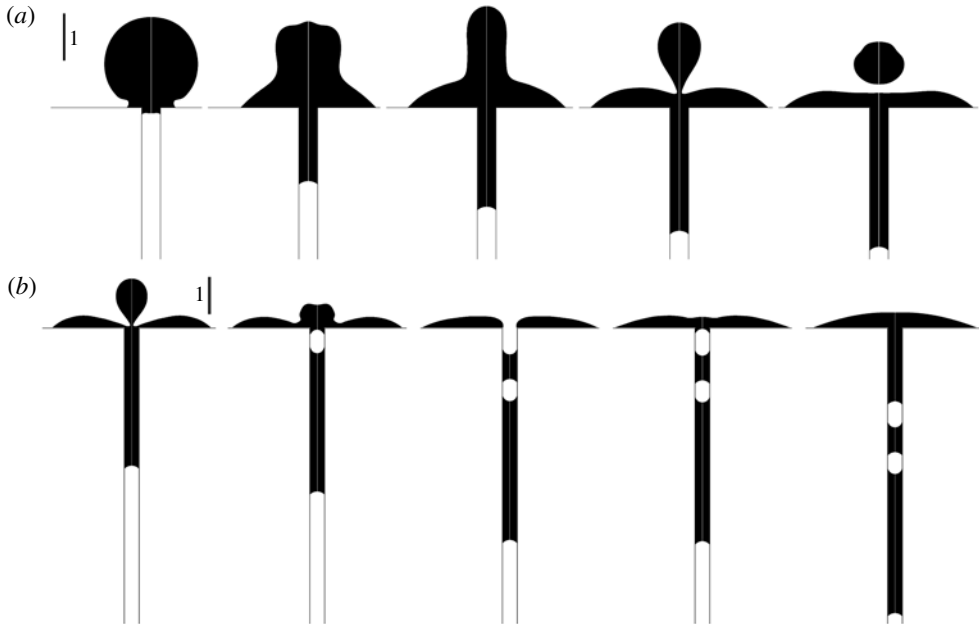
FIGURE 8. Droplet pinch-off above the substrate, for $r_t = 0.2$, $\theta_A = 40°$ and $\theta_R = 20°$. (*a*) The complete penetration regime: $Re_r = 6.9$, $We = 0.076$ and $t = 0.03$, $0.26$, $0.37$, $0.48$ and $0.57$. (*b*) The bubble entrapment regime: $Re_r = 50$, $We = 0.56$ and $t = 0.54$, $0.69$, $1.14$, $1.44$ and $4.44$.

In contrast, the values of $Ca$ in the cases shown in figures 3 and 8 are almost two orders smaller, and thus the shape of the slug front has little deformation and is always well maintained as a meniscus by the surface tension force. In addition to the interface deformation near the contact line, sufficient slug inertia is also needed to elongate the ligament. The minimum value of $Re_r$ for the occurrence of drop pinch-off inside a capillary is about 20 (figure 5). Droplet pinch-off is not observed inside the capillary at $Oh = 0.003$ and $0.007$ for the present range of $Re_r$, because of the small value of $Ca$ (the maximum value of $Ca$ is $0.027$, with $Re_r = 110$ and $We = 15$). It may occur at high $We$ and $Re_r$, which is beyond the scope of this study, however.

## 4. Inertial penetration: stagnation circle and penetration length

Flow fields at the early and late periods of inertial penetration are shown in figure 9. Here the penetration of the drop into the capillary is characterized by the presence of a high pressure zone on the solid substrate close to the capillary inlet. We find respectively a stagnation circle as a limiting streamline that separates the flow entering the capillary from that spreading outwards on the substrate (figure 9*a*). It is interesting to see that the instantaneous penetration flow rate can be significantly higher than unity (figure 4). The cause is not water-hammer, as suggested by Kogan *et al.* (2008), but straightforward incompressible hydrodynamics.

The radius of the stagnation circle is shown as a function of time in figure 10. With sufficient impact inertia (e.g. $We > 10$), the stagnation circle is more or less fixed on the solid substrate during most of the penetration period ($t < 2.5$). It turns out that when $r_t < 0.2$, the stagnation circle has a radius that remains constant for most of the transient at a value of twice the capillary radius. At the very late period of
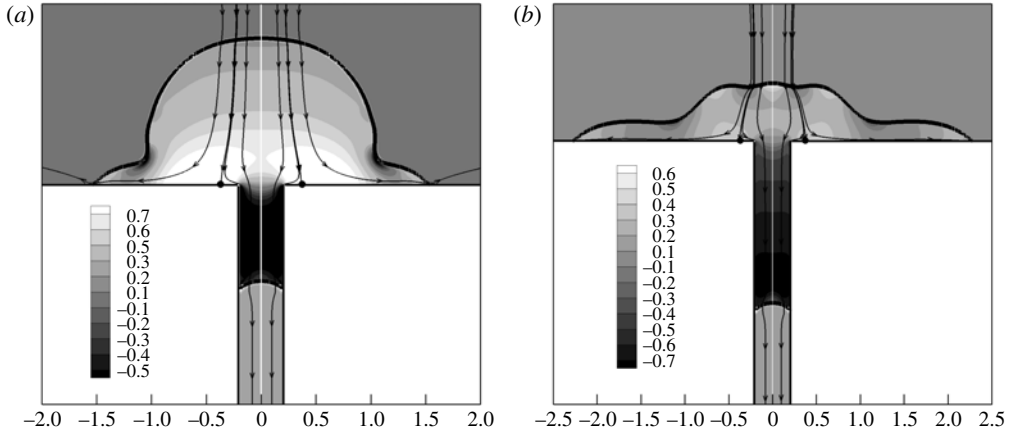
FIGURE 9. Stationary stagnation circle: flow fields at $Re_r = 62$, $We = 6.2$, $r_t = 0.2$, $\theta_A = \theta_R = 30°$. (*a*) $t = 0.65$, (*b*) $t = 1.62$. The grey scales represent the pressure contours, the thick black lines outline the drop shapes and the black dots on the substrate denote the stagnation circle.
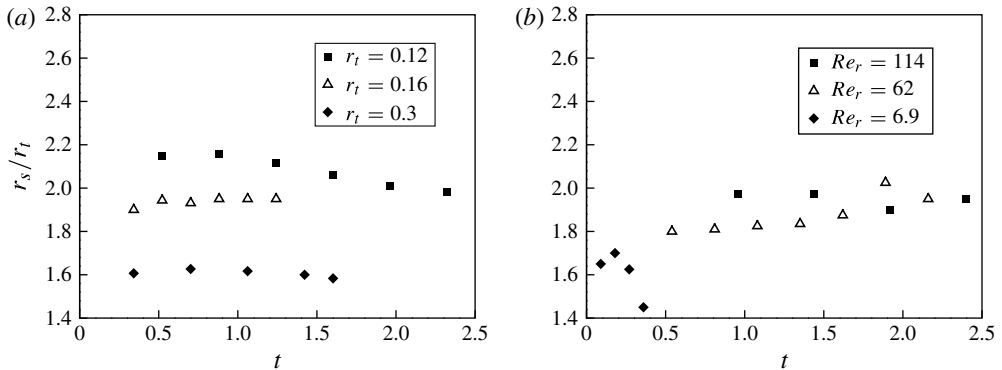


FIGURE 10. Radius of stagnation circle as a function of time. (*a*) $Re = 2810$, $We = 81$, $\theta_A = 35°$ and $\theta_R = 15°$. (*b*) $Oh = 0.008$ and $r_t = 0.2$, $\theta_A = \theta_R = 30°$.

the penetration when the top of the drop is lowered down to a height comparable to the thickness of the lamella ($t \sim 3$), the stagnation circle moves noticeably inwards. Variation of the stagnation circle is also seen when the impact velocity is small (such as $We \ll 1$) (figure 10*b*). The corresponding instantaneous flow fields of this case are shown in figure 11; further evidence is that the pressure drop induced by capillary waves can be larger than the impact pressure.

With sufficient impact inertia ($Re_r > 80$), the slug length changes slightly with $r_t$, and ranges from $3a$ to $3.4a$ (as shown in figure 12). A close inspection of reported experimental data (e.g. figure 1*e* of Delbos *et al.* 2010) shows that the corresponding slug length may also fall in this range (about $3a$). To gain insight into the origin of the slug and also for visualization of the penetration process, we initiate in the drop two sets of particles at the very beginning of the computation, and then track them in time. The two sets of particles are separated at $r = 1.3r_t$, which is estimated based on the volume of a slug of $3.4a$ in length. The evolutions of particle positions with
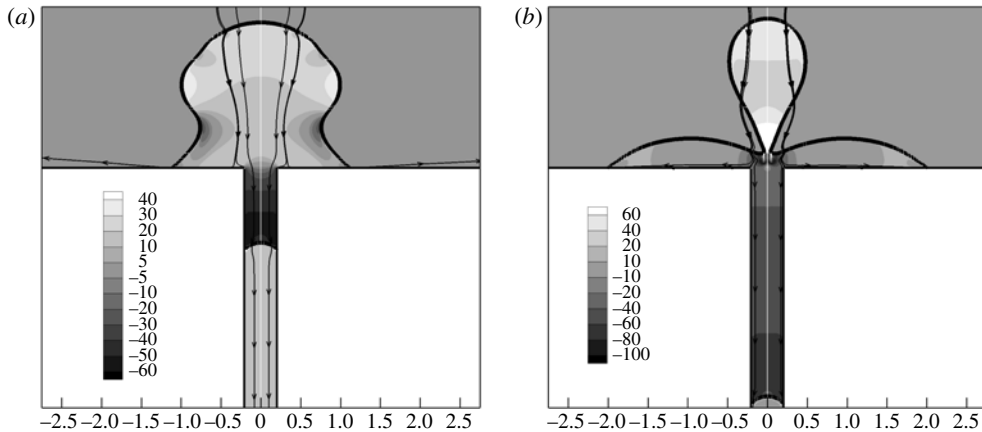
FIGURE 11. Unsteady stagnation circle: flow fields for $Re_r = 6.9$, $We = 0.076$, $r_t = 0.2$, $\theta_A = \theta_R = 30°$. (a) $t = 0.48$, (b) $t = 0.65$. The grey scales represent the pressure contours, and the thick black lines show the drop shapes. Panel (b) is at the moment just before pinch-off.
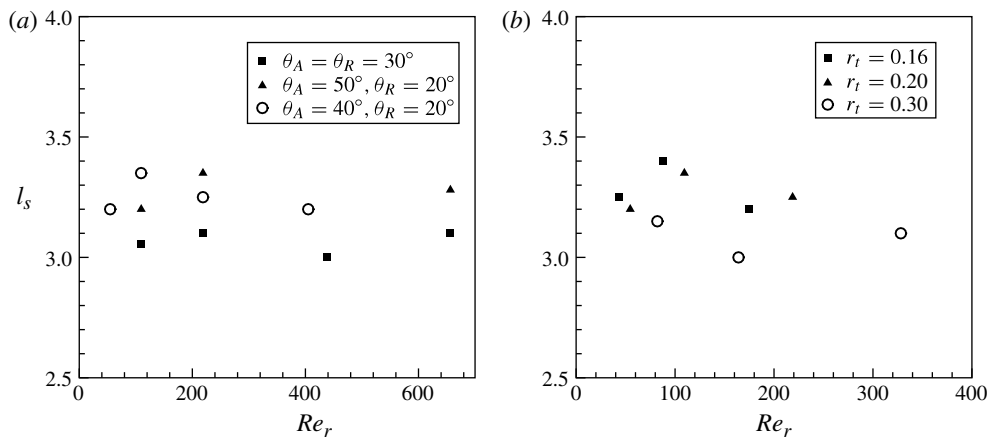


FIGURE 12. Slug length $l_S (= L_S/a)$ for $Oh = 0.007$ and (a) $r_t = 0.2$ and varied wettability, (b) $\theta_A = 40°$, $\theta_R = 20°$ and varied $r_t$. The definition of $L_S$ can be found in figure 3(g).

time for the three cases considered are shown in figure 13. At the early period of penetration, e.g. $t < 3$, the particles inside the capillary originate from the cylindrical column $r < 1.3r_t$ in all cases. When the height of the drop becomes comparable to the thickness of the lamella, a small quantity of black particles remains above the substrate and eventually resides within the lamella. This is due to the shifting of the stagnation circle towards the capillary edge. Overall we can conclude that most of the fluid penetrating into the capillary during the inertial penetration period originates from an upright cylindrical part of the drop above the capillary that is approximately $1.3r_t$ in radius.
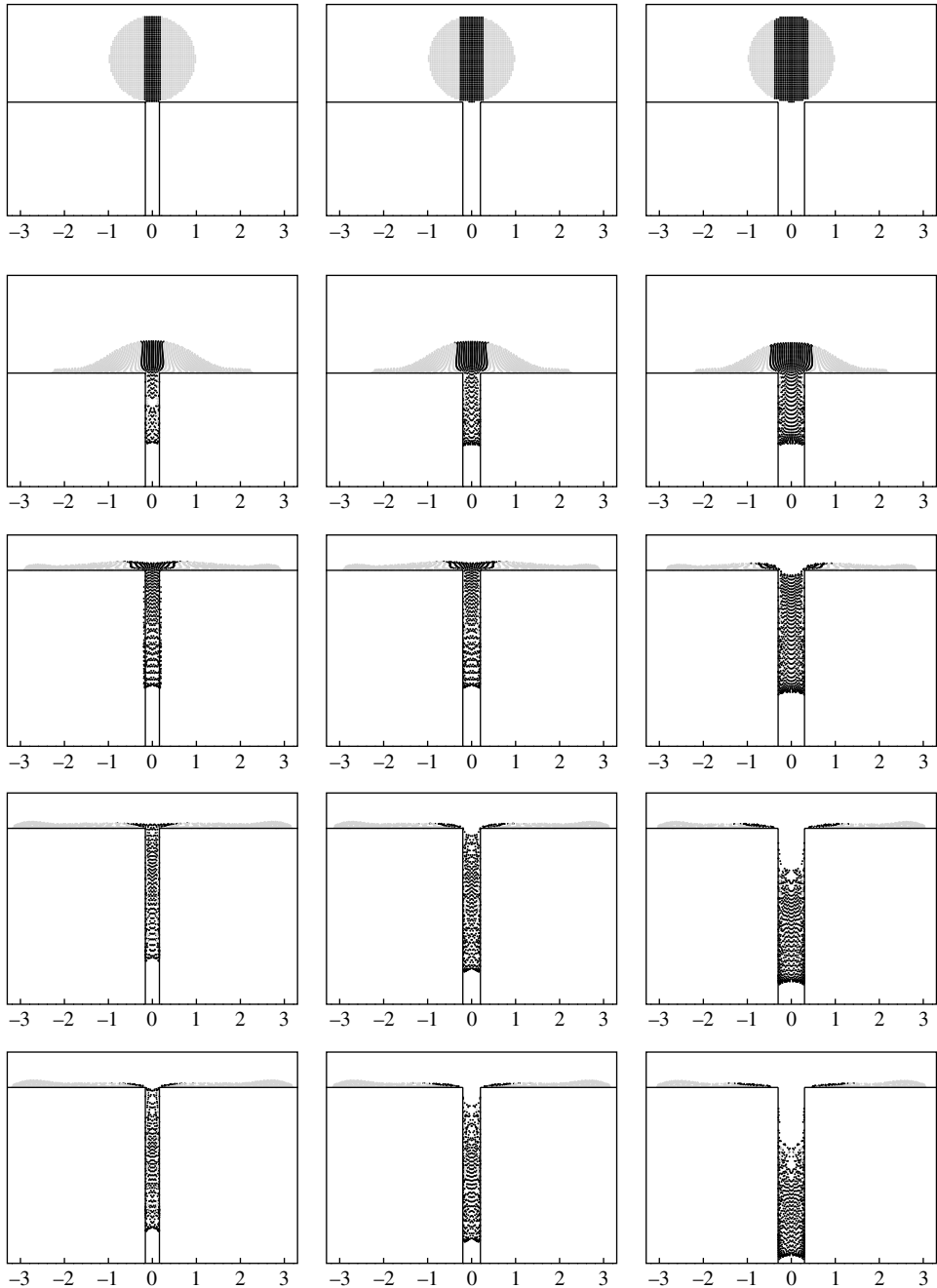
FIGURE 13. Slug formation for different capillary radii, at $Re = 684$, $We = 23$, $\theta_A = 40°$ and $\theta_R = 20°$. The columns from left to right represent numerical results for $r_t = 0.16$, $0.2$ and $0.3$, respectively. The rows from top to bottom represent the results at times $t = 0$, $1.44$, $3$, $4.44$ and $5.46$, respectively. Black dots denote the particles initially located inside the drop at $r < 1.3r_t$, while grey dots denote those located at $r > 1.3r_t$.
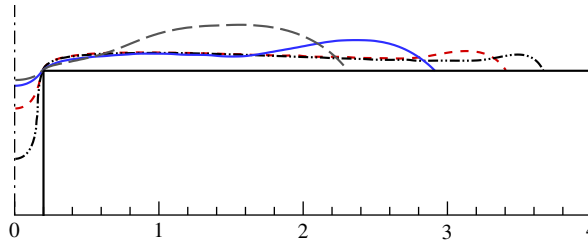
FIGURE 14. (Colour online) Snapshots at the moment just before slug formation, at $Oh = 0.004$ with different impacting velocity: $r_t = 0.2$, $\theta_A = 50°$ and $\theta_R = 30°$. The grey long-dashed line denotes results at $Re_r = 22$ and $We = 0.19$ (just beyond the onset of rupture), the solid (blue) line shows $Re_r = 44$ and $We = 0.77$, the dashed (red) line shows $Re_r = 88$ and $We = 3.1$, and the black dot-dot-dashed line shows $Re_r = 131$ and $We = 6.9$.

## 5. The mechanics of regime transitions

Figure 14 shows the snapshots of liquid rupture occurring at the edge of the capillary inlet, with a variety of different impact velocities. Again, inertia plays a crucial role here. Obviously, an increase in impact inertia encourages both the spreading out of the lamella and the penetration of liquid column, and thus promotes the occurrence of rupture. When the impact inertia is insignificant ($We < 1$), the occurrence of rupture coincides with a rapid collapse of the centre of the drop, which results from the convergence of capillary surface waves at the axis and effectively pumps the liquid into the capillary. Such collapses were observed in the fast spreading of drops at low $Oh$ (Ding & Spelt 2007a), where inertia from conversion of surface energy is the dominant factor. Besides a small value of $Oh$, a small liquid viscosity is also required for the rupture to occur for $We < 1$, such that the liquid column in the capillary has sufficient inertia ($Re_r \sim 20$ at least here). At relatively high $Oh$ ($> 0.01$), the inertial effect of curvature-driven flows becomes less significant compared to the viscous effect, and it is then reasonable to expect the impact inertia to take a more active role in the onset of occurrence of rupture, as seen in figure 5. It is also interesting to note that although the value of $\theta_A (= 50°)$ in figure 14 is different from that ($= 40°$) in figure 5, the critical condition for onset of rupture ($We = 0.19$ and $Re_r = 22$ for $Oh = 0.004$) is rather similar to the results in the latter, showing little influence of $\theta_A$ on the rupture.

In our model we do not take account of van der Waals forces, which are normally considered as the cause of rupture of a sufficiently thin liquid film on a solid substrate. For a millimetre-sized drop the mesh used in the simulation is only able to resolve a liquid film of thickness about 30 μm, far greater than the length scale ($\sim 10$ nm) at which van der Waals forces become important. Instead, when the local thickness of the liquid film is smaller than that of the diffuse interface, the effect of van der Waals forces is approximated by the diffusive fluxes of the diffuse-interface model and a rupture then occurs.

After reaching the maximum-spread area, the lamella recoils on the substrate and its radial motion can be modelled based on a balance of the force components in the cross-section (figure 15a). Since inertia is negligible, the forces are the viscous force ($\mu V_L/h_L(r_R - r_A)$), the surface tension forces at the interface ($h_L\sigma/r_A$) and at the contact line ($\sigma(\cos\theta_R - \cos\theta_A)$), where $V_L$ is the radial velocity of the lamella and is assumed to be uniform. Then, the motion of the recoiling lamella yields

$$Ca_L(r_R - r_A)/h_L + \cos\theta_R - \cos\theta_A \sim h_L/r_A, \qquad (5.1)$$
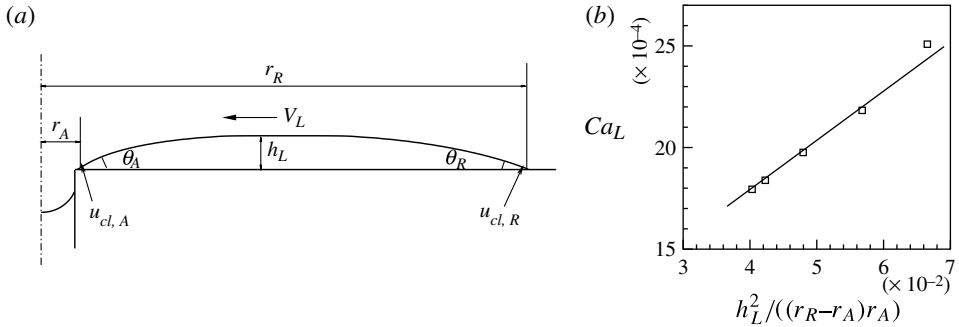
FIGURE 15. (*a*) A sketch of a receding lamella, (*b*) justifying equation (5.1) by examining a recoiling lamella for $We = 50$, $Oh = 0.01$, $r_t = 0.2$ and $\theta_A = \theta_R = 30°$. $Ca_L = \mu V_L/\sigma$, where the lamella velocity $V_L$ is approximated by $(u_{cl,A} + u_{cl,R})/2$.

where $Ca_L = \mu V_L/\sigma$. Equation (5.1) is justified by examining a recoiling lamella without contact-angle hysteresis in figure 15(*b*), in which $Ca_L$ appears to be proportional to $h_L^2/((r_R - r_A)r_A)$ at different times of recoiling motion.

The wetted area (characterized by $r_R$) is found to increase with *We* for drop impact on an impermeable substrate, while the thickness $h_L$ decreases with *We* (Clanet *et al.* 2004). Equation (5.1) suggests that the recoiling speed of the lamella would decrease with the increase in *We*. On the other hand, contact-angle hysteresis, arising from the chemical inhomogeneity or roughness of the solid substrate, hinders the motion of the lamella. In our simulations of drops at $Oh = 0.007$, re-entry with bubble entrapment occurs at $20 < Re_r < 230$ without contact-angle hysteresis (i.e. for a perfectly smooth and clean substrate), but only at $35 < Re_r < 55$ with a hysteresis of $\Delta\theta = 20°$. The quick change of normal direction to the substrate at the edge of the capillary inlet further complicates the refilling process. Although the wetting conditions of the substrate and the capillary are identical, such a transition is equivalent to modifying the advancing contact angle, roughly from $\theta_A$ to $\theta_A + 45°$ (as shown in figure 16). This consequently leads to an effective contact-angle hysteresis at the capillary inlet, even for cases with $\theta_A = \theta_R$. As a result, lamellae with sufficient recoiling inertia, e.g. for drops with low *Oh* and *We*, could refill the capillary. Otherwise the contact line is then pinned at the sharp edge of the capillary inlet. This also explains why the penetration regime transits from the re-entry with bubble entrapment to the partial penetration with a slug with increasing impact speed (see figure 5), rather than the other way around.

Figure 17 shows the snapshot at a time before a bubble is entrapped. The refilling leads to the occurrence of a neck near the capillary inlet, and the neck will keep shrinking and eventually coalesce to minimize the surface energy. During this process a little amount of gas is squeezed out of the bubble and generates a vortex ring above the neck. The size of the bubble is roughly the distance that the slug moves in the capillary before the refilling event, and is mainly a function of $Re_r$; detailed analysis is provided in §6.

Figure 18(*a*) shows the spreading dynamics of the drop on the solid substrate in terms of contact-line position as a function of time. The radius of the wetted area approximately yields a power-law relation $R \sim t^{1/2}$, indicating the inertia-dominant spreading process and being in agreement with theoretical analysis and experimental observations. For example, with very slow impact speed the $R \sim t^{1/2}$ relation was seen for $Oh < 0.01$ (Biance *et al.* 2004; Ding & Spelt 2007*a*), while with high
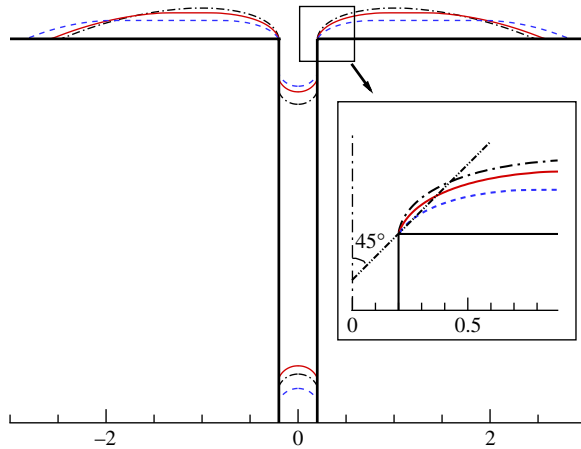
FIGURE 16. (Colour online) Settled slug and lamella in the slug regime, with $\theta_A = 40$ and $\theta_R = 20°$. The black dot-dashed line represents the results at $We = 2.1$ and $Re_r = 41$ (nearly at the onset of re-entry with bubble entrapment), the solid (red) line shows $We = 3.7$ and $Re_r = 55$, and the dashed (blue) line shows $We = 15$ and $Re_r = 109$. The black dot-dot-dashed line in the zoomed view represents the tangent plane to the edge of capillary inlet.
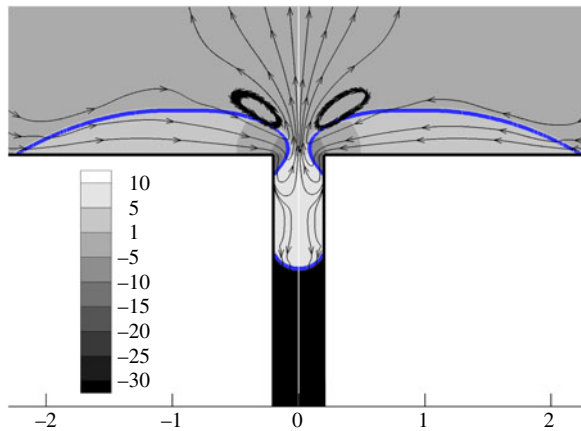


FIGURE 17. (Colour online) Onset of bubble entrapment at $r_t = 0.2$, $\theta_A = \theta_R = 30°$, $Re_r = 109$ and $We = 15$. The grey scales represent the pressure distribution and the thick grey (blue) line represents the interface.

impact velocity this relation holds in the so-called kinematic period regardless of the physical properties of the drop and the wettability (Rioboo, Marengo & Tropea 2002). Figure 18(*b*) shows the maximum radius of wetted area $R_{max}$ as a function of $Re$. Their correlation can be approximated by $R_{max} \sim Re^{0.18}$, agreeing with the prediction of a viscous dissipation model (Clanet *et al.* 2004) ($R_{max} \sim Re^{1/5}$) for drop impact on an impermeable substrate. Overall it appears that the presence of the capillary has almost no effect on the contact-line dynamics of the drop spreading on the solid substrate, primarily because only a limited amount of the drop (less than 10 % for $r_t \leqslant 0.2$) is lost into the capillary during the impact process.
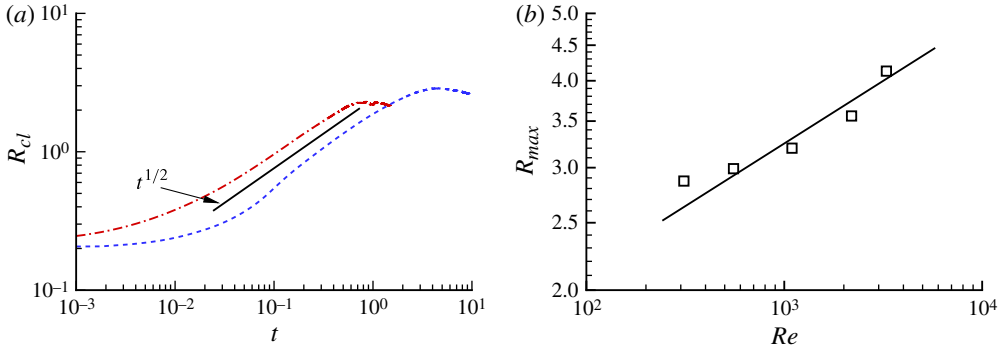
FIGURE 18. (Colour online) Spreading of the drop on the solid substrate: (*a*) contact-line position $R_{cl}$ as a function of time with $r_t = 0.2$, $\theta_A = \theta_R = 30°$, and (*b*) maximum radius of the wetted area $R_{max}$ as a function of $Re$. In (*a*), the dot-dashed (red) line represents the case at $Re_r = 6.9$ and $We = 0.076$ and the dashed (blue) line represents the the case at $Re_r = 62$ and $We = 6.2$. In (*b*), the squares represent numerical results and the solid line represents a fitting of $R_{max} \sim Re^{0.18}$.

## 6. Discussion

The dynamics of the liquid column in the capillary is analysed based on a scaling argument of the forces exerted on the liquid column. We consider a liquid column of length $LR_t$ moving in the capillary with a velocity of Poiseuille flow profile, of which the average value is $V_pU$; here a positive $V_p$ suggests a downward motion of the liquid column. The forces exerted by the surrounding fluids and the capillary on the liquid column are as follows: the impact pressure $p(t)\pi R_t^2 \rho U^2$ where the coefficient $p(t)$ damps gradually with time, the viscous shear stress from the capillary wall $8V_pL\pi\mu UR_t$, the effect of gravity $L\rho\pi gR_t^3$, the capillary forces associated with the wettability $2\pi R_t\sigma\cos\theta$ where $\theta$ is the contact angle (we do not consider contact-angle hysteresis here, so $\theta = \theta_A = \theta_R$). Then the equation of motion for the liquid column yields

$$L\frac{\mathrm{d}V_p}{\mathrm{d}t} = p(t) + \frac{2}{We_r}\cos\theta - \frac{8}{Re_r}LV_p + \frac{L}{Fr_r}. \tag{6.1}$$

A similar scaling argument has been successfully used by Zhmud, Tiberg & Hallstensson (2000) in the analysis of the dynamics of capillary rise. We use this model to quantify the penetration of the drop in the three periods as shown in figure 4, and it can be further simplified according to the specific dominant forces in the respective period.

In the penetration period, the infiltration rate $V_p$ can be approximated by the time derivative of the liquid column length, $\dot{L}$. At very early times, the effect of the impact pressure is expected to be dominant, but reduces with time. For example, Eggers *et al.* (2010) found that the impact pressure of drop impact on a solid wall damps as a power law of time such that $p(t) \sim t^{-0.5}$. This fact complicates the analysis of the dynamics of the liquid column at early penetration. At later times, when the effect of the impact pressure is weak and surface tension and viscous force become important, the variation of the liquid column length yields

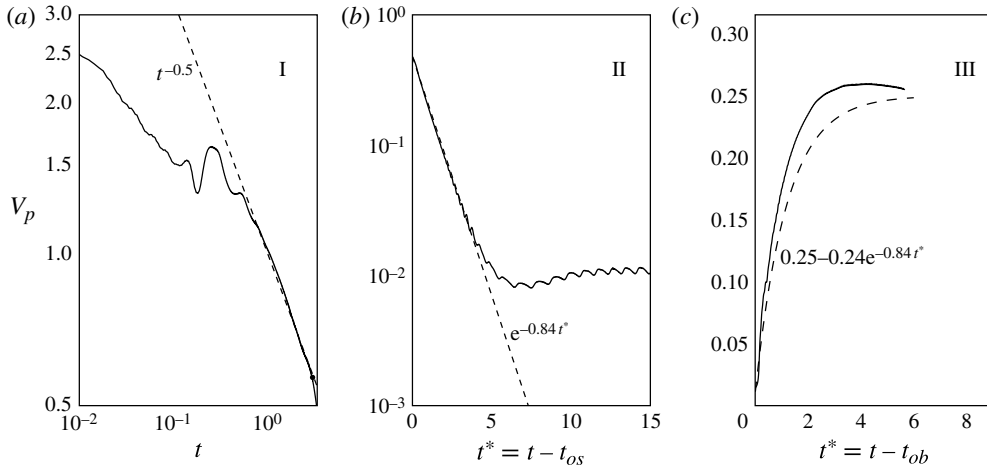$$\frac{2}{We_r}\cos\theta \sim \frac{8}{Re_r}L\dot{L}. \tag{6.2}$$

FIGURE 19. Three periods in penetration dynamics: $Re_r = 62$, $We = 6.2$, $r_t = 0.2$, $\theta_A = \theta_R = 30°$. The notations I, II and III represent the periods of inertial penetration (*a*), moving slug (*b*) and bubble entrapment (*c*), respectively. The solid lines represent numerical results and the dashed lines represent results from the scaling arguments by (6.1); $t_{os}$ and $t_{ob}$ represent the time at the onset of slug formation and bubble formation, respectively. The thick spot in (*a*) denotes the transition to slug formation. This is the same case as in figure 4.

Thus, the growth rate of the liquid column satisfies $\dot{L} \sim \sqrt{((Re_r \cos\theta)/(8We_r))}t^{-0.5}$. The infiltration rate from numerical results is plotted as a function of time in figure 19(*a*), in which the results of $V_p$ are well fitted by a straight line of slope $-0.5$ in logarithmic scales when $t > 1$ and before the onset of slug formation, in good agreement with the scaling argument in (6.2).

When the liquid column in the capillary becomes a moving slug (as seen in figure 3*e*), the driving forces are inertia, viscous force and gravitational force. In particular, the first two are the dominant forces for relatively large $V_p$, and thus the slug motion is governed by

$$L\frac{\mathrm{d}V_p}{\mathrm{d}t} \sim -\frac{8}{Re_r}LV_p. \tag{6.3}$$

This suggests $V_p \sim \mathrm{e}^{-8t/Re_r}$. For very slow slug motion, the gravitational force is balanced by the viscous force, and the velocity at equilibrium $V_{eqm}$ would be $V_{eqm} = Re_r/(8Fr_r)$, which is about 0.019 for the case in figure 19. Figure 19(*b*) shows the dimensionless $V_p$ versus $t^*$ for the moving slug period from the numerical simulations, where $t^* = t - t_{os}$ and $t_{os}$ denotes the time at the onset of slug formation. Note that $V_p$ is obtained by numerically differentiating the position of the slug front in a regular time interval, and the numerical error in this post-processing results in the oscillations in $V_p$ (particularly when $V_p$ is very small), which has nothing to do with the accuracy of the solution. Clearly the slug velocity is damped exponentially at early times after the slug is formed, and then asymptotically transits to a constant value, as expected by the scaling argument. Numerical simulations show an exponent of 0.84 for the damping and $V_p = 0.012$ at late times, compared to 0.65 and 0.019 from the theoretical analysis, respectively.

The refilling, as seen in figure 3(*g,h*), results in an imbalance of the capillary pressures between the front of the liquid column and the capillary inlet, and

consequently exerts an impulsive force pulling the liquid into the capillary. If the variation of length of the liquid column $L$ is neglected, the motion of the liquid column yields

$$\frac{\mathrm{d}V_p}{\mathrm{d}t^*} = \frac{2}{LWe_r}\cos\theta - \frac{8}{Re_r}V_p, \tag{6.4}$$

which is an ordinary differential equation with boundary conditions $V_{p,0} = 0.012$ at $t = 0$ and $V_{p,\infty} = ((2/LWe_r)\cos\theta)/(8/Re_r)$ at $t \to \infty$; $t^* = t - t_{ob}$ and $t_{ob}$ represents the time at the onset of bubble formation. The solution of (6.4) can be obtained analytically:

$$V_p = V_{p,\infty} - (V_{p,\infty} - V_{p,0})\mathrm{e}^{-8t^*/Re_r}. \tag{6.5}$$

If we approximate the viscous force by setting $8/Re_r = 0.84$ (which is obtained by fitting exponential damping in the moving slug period), then $V_{p,\infty} = 0.251$, in agreement with the numerical results ($V_{p,\infty} = 0.255$). Figure 19(c) shows the comparison between numerical simulations and theoretical analysis for the bubble entrapment period.

## 7. Drop impact on embedded annular capillaries

We consider here drop impact on a substrate with embedded annular capillaries, which serves as a model of a porous substrate. Figure 20 shows a typical example, in which impact inertia is rather significant. The effective permeability of the embedded annular capillaries is about 0.45, much larger than that of a single capillary (approximately 0.01 to 0.02 for $r_t = 0.2$ to 0.3). As a result the infiltration in the embedded annular capillaries significantly affects the drop spreading on the porous substrate. It is shown in figure 20 that the maximum radius of the lamella is just slightly bigger than that of the original drop, and there is almost no recoiling. Clearly, inertia plays a dominant role in the infiltration process, and leads to rapid penetrations: the drop is absorbed by the substrate within a time of approximately 2 (as shown in the figure 20), which is equivalent to the time for the drop to fall freely by distance equal to a drop diameter. In particular, in the three annular capillaries close to the axis, the slug lengths are roughly proportional to the lengths of annular liquid columns of the initial drop above the respective capillaries. This suggests that the porous surface is probably divided into two infiltration regions: the impact-dominated one ($r < a$) and the spreading-dominated one ($r > a$). Particle tracking (not shown here) reveals that at early times of penetration (up to figure 20c), geometrically a cylindrical column of the initial drop ($r < 1.3r_t$) infiltrates into the centre capillary, which is similar to the drop impact on a single capillary; then a small portion diverts to the neighbouring annular capillary at the same time as the shifting of the related stagnation circle. At the end of the penetration period ($t \sim 4$), it is interesting to notice that most of the drop has been absorbed by the capillaries; remaining on the porous substrate are a few annular liquid threads, which could further break up into a necklace, but this is outside our present focus.

## 8. Conclusions

The dynamics of infiltration and spreading after a drop impacting onto a hydrophilic substrate with single capillary has been investigated numerically by a diffuse-interface method. The penetration regimes observed in experiments (Delbos *et al.* 2010) have been reproduced and generalized by mapping numerical results in the $We - Re_r$ plane.
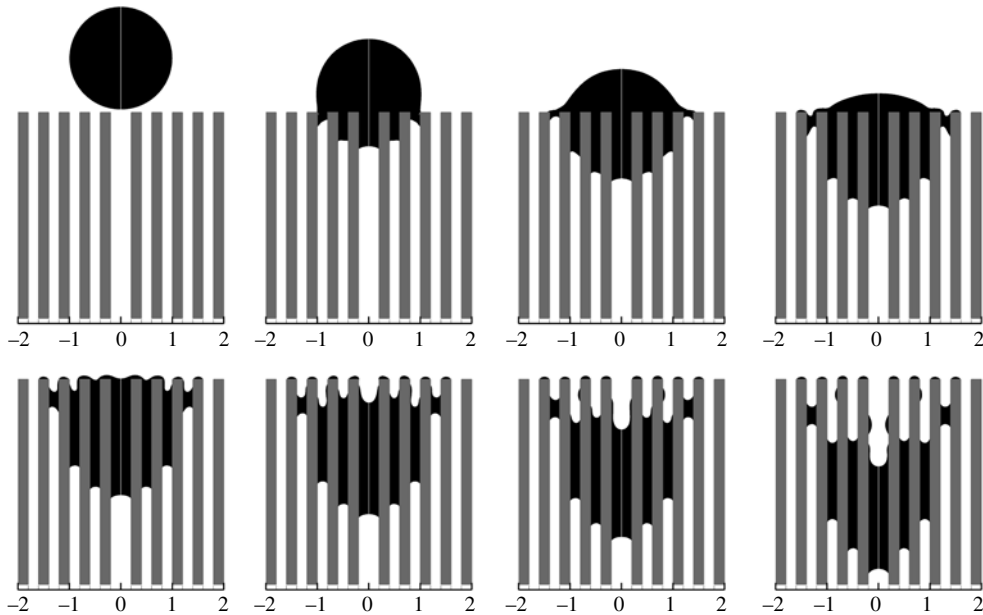
FIGURE 20. Drop impact on embedded annular capillaries. $Re = 1094, We = 59$ and $\theta_A = \theta_R = 30°$. The size of the gaps are uniform, i.e. 0.2, except the centre capillary, of which the radius is 0.2. Snapshots at $t = 0$, 0.64, 1.28, 1.92, 2.56, 3.2, 4.16 and 6.4, respectively.

Interesting phenomena – droplet ejections – have been observed not only above the substrate, but also inside the capillary, though the related mechanisms are shown to be very different. Inertia appears to be crucial in all these events: inertia from the conversion of surface energy is more important in droplet ejection above the substrate, while sufficient impact inertia is a necessity for droplet ejection inside the capillary. The significance of impact inertia in the slug formation is reflected by a spatial anchoring of stagnation region with time. As a result, the amounts of liquid inside the slug are found to come from an upright cylinder above the capillary. This is in agreement with the hypothesis of Delbos *et al.* (2010), but the radius of the cylinder is 30 % greater than the capillary radius. This observation also provides a reasonable interpretation of the previous experimental observations, e.g. the unusually large infiltration rate (Kogan *et al.* 2008) and the constant slug volume at sufficiently large $Re_r$ (Delbos *et al.* 2010). Inertia and contact-angle hysteresis are shown to be the most important factors in the transition of penetration regimes; the latter has an especially significant effect on the transition to the regime of partial penetration as a slug. Finally an attempt is made to use embedded annular capillaries to model porous surfaces, and two infiltration regions have been identified: the impact-dominant region and the spreading-dominant region, distinguished by the initial drop radius.

### Acknowledgements

## REFERENCES

ALLEBORN, N. & RASZILLIER, H. 2004 Spreading and sorption of a droplet on a porous substrate. *Chem. Engng Sci.* **59**, 2071–2088.

BIANCE, A.-L., CLANET, C. & QUÉRÉ, D. 2004 First steps in the spreading of a liquid droplet. *Phys. Rev. E* **69**, 016301.

BLANCHETTE, F. & BIGIONI, T. P. 2006 Partial coalescence of drops at liquid interfaces. *Nature Phys.* **2**, 254–257.

CLANET, C., BEGUIN, C., RICHARD, D. & QUÉRÉ, D. 2004 Maximal deformation of an impacting drop. *J. Fluid Mech.* **517**, 199–208.

CLARKE, A., BLAKE, T. D., CARRUTHERS, K. & WOODWARD, A. 2002 Spreading and imbibition of liquid droplets on porous surfaces. *Langmuir* **18**, 2980.

DAVIS, S. H. & HOCKING, L. M. 1999 Spreading and imbibition of viscous liquid on a porous base. *Phys. Fluids* **11**, 48–57.

DAVIS, S. H. & HOCKING, L. M. 2000 Spreading and imbibition of viscous liquid on a porous base. Part II. *Phys. Fluids* **12**, 1646–1655.

DELBOS, A., LORENCEAU, E. & PITOIS, O. 2010 Forced impregnation of a capillary tube with drop impact. *J. Colloid Interface Sci.* **341**, 171–177.

DENESUK, M., SMITH, G. L., ZELINSKI, B. J. J., KREIDL, N. J. & UHLMANN, D. R. 1993 Capillary penetration of liquid droplets into porous materials. *J. Colloid Interface Sci.* **158**, 114–120.

DING, H., LI, E. Q., ZHANG, F., SUI, Y., SPELT, P. D. M. & THORODDSEN, S. T. 2011 Ejection of small droplets in rapid droplet spreading. Under consideration for publication in *J. Fluid Mech.* (submitted).

DING, H. & SPELT, P. D. M. 2007*a* Inertial effects in droplet spreading: a comparison between diffuse interface and level-set simulations. *J. Fluid Mech.* **576**, 287–296.

DING, H. & SPELT, P. D. M. 2007*b* Wetting condition in diffuse interface simulation of contact line motion. *Phys. Rev. E* **75**, 046708.

DING, H. & SPELT, P. D. M. 2008 Onset of motion of a 3D droplet on a wall in shear flow at moderate Reynolds numbers. *J. Fluid Mech.* **599**, 341–362.

DING, H., SPELT, P. D. M. & SHU, C. 2007 Diffuse interface model for incompressible two-phase flows with large density ratios. *J. Comput. Phys.* **226**, 2078–2095.

EGGERS, J., FONTELOS, M. A., JOSSER, C. & ZALESKI, S. 2010 Drop dynamics after impact on a solid wall: theory and simulations. *Phys. Fluids* **22**, 062101.

FEDORCHENKO, A. I., WANG, A.-B. & WANG, Y.-H. 2005 Effect of capillary and viscous forces on spreading of a liquid drop impinging on a solid surface. *Phys. Fluids* **17**, 093104.

DE GENNES, P. G. 1985 Wetting: statistics and dynamics. *Rev. Mod. Phys.* **57**, 827–863.

HILPERT, M. & BEN-DAVID, A. 2009 Infiltration of liquid droplets into porous media: effects of dynamic contact angle and contact angle hysteresis. *Intl J. Multiphase Flow* **35**, 205–218.

HOLMAN, R. K., CIMA, M. J., UHLAND, S. A. & SACHS, E. 2002 Spreading and infiltration of inkjet-printed polymer solution droplets on a porous substrate. *J. Colloid Interface Sci.* **249**, 432–440.

JACQMIN, D. 1999 Calculation of two-phase Navier–Stokes flows using phase-field modelling. *J. Comput. Phys.* **155**, 96–127.

JACQMIN, D. 2000 Contact-line dynamics of a diffuse fluid interface. *J. Fluid Mech.* **402**, 57.

KOGAN, V., JOHNSON, E. & SCHUMACHER, P. 2008 Capillary flow of liquid under droplet impact conditions. In *22nd European Conference on Liquid Atomization Spray Systems, Lake Como, Italy*. Paper ID ILASS08-A131.

LEE, M., CHANG, Y. S. & KIM, H. Y. 2010 Drop impact on microwetting patterned surfaces. *Phys. Fluids* **22**, 072101.

LEMBACH, A. N., TAN, H. B., ROISMAN, I. V., ROISMAN, T. G., ZHANG, Y., TROPEA, C. & YARIN, A. L. 2010 Drop impact, spreading, splashing, and penetration into electrospun nanofibre mats. *Langmuir* **26**, 9516–9523.

MARMUR, A. & COHEN, R. D. 1997 Characterization of porous media by the kinetics of liquid penetration: the vertical capillaries model. *J. Colloid Interface Sci.* **189**, 299–304.

RIOBOO, R., ADAO, M. H., VOUÉ, M. & DE CONINCK, J. 2006 Experimental evidence of liquid drop breakup in complete wetting experiments. *J. Mater. Sci.* **41**, 5068–5080.

RIOBOO, R., MARENGO, M. & TROPEA, C. 2002 Time evolution of liquid drop impact onto solid, dry surfaces. *Exp. Fluids* **33**, 112–124.

ROUX, D. C. D. & COOPER-WHITE, J. J. 2004 Dynamics of water spreading on a glass surface. *J. Colloid Interface Sci.* **277**, 424–436.

SEPPECHER, P. 1996 Moving contact lines in the Cahn–Hilliard theory. *Intl J. Engng Sci.* **34**, 977–992.

SEVENO, D., LEDAUPHIN, V., MARTIC, G., VOU, M. & DE CONINCK, J. 2002 Spreading drop dynamics on porous surfaces. *Langmuir* **18**, 7496–7502.

SIVAKUMAR, D., KATAGIRI, K., SATO, T. & NISHIYAMA, H. 2005 Spreading behaviour of an impacting drop on a structured rough surface. *Phys. Fluids* **17**, 100608.

WASHBURN, E. W. 1921 The dynamics of capillary flow. *Phys. Rev.* **17**, 273.

XU, L. 2005 Liquid drop splashing on smooth, rough, and texture surfaces. *Phys. Rev. E* **75**, 056316.

ZHANG, F. H., LI, E. Q. & THORODDSEN, S. T. 2009 Satellite formation during coalescence of unequal size drops. *Phys. Rev. Lett.* **102**, 104502.

ZHMUD, B. V., TIBERG, F. & HALLSTENSSON, K. 2000 Dynamics of capillary rise. *J. Colloid Interface Sci.* **228**, 263–269.